

See discussions, stats, and author profiles for this publication at: <https://www.researchgate.net/publication/231629120>

The $\tilde{A}^2E/\tilde{B}^2B_2$ Photoelectron Bands of Allene beyond the Linear Coupling Scheme: An ab Initio Dynamical Study Including All Fifteen Vibrational Modes†

ARTICLE in THE JOURNAL OF PHYSICAL CHEMISTRY A · MARCH 2001

Impact Factor: 2.69 · DOI: 10.1021/jp003727i

CITATIONS

70

READS

12

5 AUTHORS, INCLUDING:



Susanta Mahapatra

University of Hyderabad

114 PUBLICATIONS 1,637 CITATIONS

SEE PROFILE



Hans-Dieter Meyer

Universität Heidelberg

245 PUBLICATIONS 9,847 CITATIONS

SEE PROFILE



Horst Köppel

Universität Heidelberg

240 PUBLICATIONS 5,958 CITATIONS

SEE PROFILE

The $\tilde{A}^2E/\tilde{B}^2B_2$ Photoelectron Bands of Allene beyond the Linear Coupling Scheme: An ab Initio Dynamical Study Including All Fifteen Vibrational Modes[†]

S. Mahapatra,^{‡,§} G. A. Worth,[‡] H.-D. Meyer,[‡] L. S. Cederbaum,[‡] and H. Köppel^{*,‡}

Department of Theoretical Chemistry, University of Heidelberg, Im Neuenheimer Feld 229, D-69120 Heidelberg, Germany, and School of Chemistry, University of Hyderabad, Hyderabad 500 046, India

Received: October 11, 2000; In Final Form: January 9, 2001

In an earlier publication [*J. Chem. Phys.* **1999**, *111*, 10452] we theoretically investigated the photoelectron spectrum of allene ($C_3H_4^+$) pertinent to the $\tilde{A}^2E/\tilde{B}^2B_2$ interacting electronic manifold of its radical cation ($C_3H_4^+$). Employing a linear vibronic coupling scheme it was demonstrated that in addition to the $E \otimes B$ Jahn–Teller activity within the $2e$ electronic manifold, there is a strong $(E \otimes B) + E$ pseudo-Jahn–Teller interaction with the \tilde{B}^2B_2 electronic state, which causes the diffuse structures observed at high energies. Here, the same photoelectron spectrum is reinvestigated including all fifteen vibrational degrees of freedom of the system and a higher order coupling scheme. The coupling parameters of the Hamiltonian are calculated by ab initio methods. The photoelectron band is calculated by the wave packet propagation method within the multiconfiguration time-dependent Hartree (MCTDH) scheme and compared with the experimental results of Baltzer et al. [*Chem. Phys.* **1995**, *196*, 551]. The progressions at low energies are identified unambiguously by calculating the “stick” vibronic spectrum within the \tilde{A}^2E electronic manifold, considering five relevant vibrational modes, and the effect of the higher order couplings is clearly demonstrated. The calculations show that it is necessary to re-assign the progressions in the low-energy region of the spectrum to the vibrational mode ν_3 , which is of C=C stretching and H–C–H bending character and the combination of symmetric (ν_2) and antisymmetric (ν_7) H–C–H bending vibrational modes. In addition, we report on the time-dependent nuclear dynamics by snapshots of the time-evolved wave packet and by the diabatic electronic populations.

I. Introduction

Valence photoelectron spectroscopy is a powerful and robust tool to investigate the vibrational energy level structure of ionized and neutral molecules,^{1–6} and over the past few decades this tool has been applied to a variety of organic hydrocarbons in order to record the energy spectrum of the corresponding cations. The development of ZEro Kinetic Energy (ZEKE) spectroscopy was a major step forward in this field, enabling spectra to be recorded with an unprecedented energy resolution and rotationally resolved transitions.^{4,6} For almost all molecular systems photoelectron transitions occur to more than one final electronic state, and these are often coupled together through the nuclear motion (known as *vibronic coupling*). The resulting energy level spectrum then bears the signature of interesting nonadiabatic effects. In particular, the importance of *conical intersections* of molecular electronic states in this context clearly emerged^{7,8} and has received increasing attention in recent years.^{9–12} A well-known subclass of conically intersecting potential energy surfaces is represented by Jahn–Teller (JT) systems,^{13,14} in which the symmetry-enforced electronic degeneracy is unstable (for nonlinear conformations) with respect to suitable symmetry-reducing nuclear displacements. Another subclass deals with the interaction between a degenerate and a nondegenerate electronic state. These are identified as pseudo-Jahn–Teller (PJT) systems in the literature.^{8,15–17} Such vibronic interactions of molecular electronic states lead to a breakdown

of the Born–Oppenheimer approximation, and in dealing with them in theoretical studies, one needs to monitor the nuclear motion simultaneously on more than one electronic surface. The ubiquity of conical intersections in this regard has been explicitly demonstrated by several authors.^{7–12}

Allene ($C_3H_4^+$) is an organic hydrocarbon with 15 normal vibrational modes and belongs to the D_{2d} symmetry point group. The 15 vibrational modes of allene have the following irreducible representations:¹⁸

$$\Gamma = 3A_1 + B_1 + 3B_2 + 4E \quad (1)$$

The valence photoelectron spectrum of allene ($C_3H_4^+$) has been studied by several experimental groups.^{1,19–24} The ground and the first excited states of the allene radical cation ($C_3H_4^+$) are of the 2E type. Each of them is orbitally degenerate at the D_{2d} symmetry configuration. The symmetric direct product of the E representation in the D_{2d} point group decomposes as

$$[E \times E] = A_1 + B_1 + B_2 \quad (2)$$

The vibrational modes of A_1 symmetry cannot destroy the degeneracy of the 2E electronic manifold, whereas the vibrational modes of B_1 and B_2 symmetry can lift this degeneracy, and thus display $E \otimes B$ JT activity.^{8,13,14,25} The participation of nondegenerate vibrational modes in the JT activity is quite rare and can be encountered in molecules possessing only a two- or four-fold axis of symmetry, for example, those belonging to the D_{2d} , D_{4h} , or D_{4d} symmetry point groups. The degenerate vibrational modes (E) do not participate in the nuclear dynamics

[†] Part of the special issue “Edward W. Schlag Festschrift”.

[‡] University of Heidelberg.

[§] University of Hyderabad.

either in the \tilde{X}^2E or in the \tilde{A}^2E electronic manifold of $C_3H_4^+$. However, because of the selection rule (in the D_{2d} point group)

$$[E \times B_2] = E \quad (3)$$

they can couple the \tilde{A}^2E electronic manifold with the next higher \tilde{B}^2B_2 electronic state in first order and display PJT activity. PJT interactions induced by degenerate vibrational modes have been encountered in other situations.^{15,16} The $\tilde{A}^2E/\tilde{B}^2B_2$ photoelectron spectrum of allene represents an interesting example in which to study the interplay between the JT and PJT effects, involving nondegenerate JT active vibrational modes.

The experimental $\tilde{A}^2E/\tilde{B}^2B_2$ photoelectron band of allene shows resolved progressions at low energies and a highly diffuse structure at high energies.^{22–24} Woywod and Domcke²⁶ carried out theoretical investigations to study the JT effect in the \tilde{A}^2E ionic manifold. With a two-state and four-mode model Hamiltonian and a linear vibronic coupling (LVC) scheme they could reproduce most of the low-energy part of the $\tilde{A}^2E/\tilde{B}^2B_2$ photoelectron band recorded by Yang et al.²² Due to the strength of the coupling parameter, they assigned the low-energy structures in this photoelectron band as progressions along the symmetric and the antisymmetric H–C–H bending vibrational modes ν_2 (A_1) and ν_7 (B_2), respectively. This assignment, however required a significant empirical adjustment of the linear vibronic coupling constants and vibrational frequencies for the ν_2 and ν_7 modes on excitation. However, we note that Yang et al.²² had assigned the structure as progressions along the ν_2 and ν_3 vibrational modes.

In ref 17 we have investigated the $\tilde{A}^2E/\tilde{B}^2B_2$ photoelectron band of $C_3H_4^+$ by constructing a three-state and ten-mode model Hamiltonian within the LVC scheme by an ab initio quantum dynamical approach. Our results were shown to compare well with the high-resolution He I excited recording of Baltzer et al.²³ The main focus in this study was to clearly demonstrate the interplay between the JT and the PJT effects in the photoelectron transition in allene and we, as well as Baltzer et al.,²³ followed the assignments of Woywod and Domcke for the low-energy progressions in the photoelectron band.

In the present article we set out to reinvestigate the $\tilde{A}^2E/\tilde{B}^2B_2$ photoelectron band of allene with a model Hamiltonian including all 15 vibrational modes and a higher order coupling scheme. The higher order coupling constants are calculated by the ab initio outer valence Green's function (OVGF) method.^{27,28} With the inclusion of the quadratic and the bilinear coupling terms in the Hamiltonian the progressions in the low-energy part of the envelope are shown to be formed by the vibrational modes ν_3 and $\nu_2 + \nu_7$. These progressions are unambiguously identified by calculating the "stick" vibronic spectrum of the JT interacting \tilde{A}^2E electronic manifold. The full three-state and fifteen-mode spectrum is computed by wave packet propagation methods within the multiconfiguration time-dependent Hartree (MCTDH) scheme.²⁹ The MCTDH scheme has been found to be very successful in the treatment of a variety of problems including reactive and surface scattering, photodissociation and the photoexcitation of vibronically coupled systems. For further details of the method and its applications see, for example, the recent review³⁰ and references therein. Of particular interest in this context are a set of studies on the photoexcitation of the pyrazine molecule. There, the full quantum mechanical nuclear dynamics of all 24 vibrational modes in two coupled electronic states have been accurately treated.^{31–33} The present example is an extension of this treatment with three interacting electronic states involved in the nuclear dynamics.

The paper is organized in the following way. In section II we describe the theoretical background where the model diabatic vibronic Hamiltonian, computational details of the photoelectron spectrum, wave packet calculations by the MCTDH scheme, and the ab initio computations of the coupling constants entering the Hamiltonian are presented. In section III the theoretical photoelectron spectrum is shown and discussed, and compared with the experimental recording. The time-dependent dynamics for the ultrafast $\tilde{A}^2E \leftarrow \tilde{B}^2B_2$ interstate conversion is then illustrated in terms of the diabatic electronic populations and snapshots of the wave packet along the most relevant normal mode coordinate. Finally, summarizing remarks are presented in section IV.

II. Theoretical Background

A. Vibronic Hamiltonian and the Photoelectron Spectrum.

The photoexcitation process of allene is described by a Franck–Condon (FC) transition from its electronic ground state to the $\tilde{A}^2E/\tilde{B}^2B_2$ interacting electronic manifold of the radical cation ($C_3H_4^+$). This involves excitation of an electron from the $1e/3b_2$ valence orbitals of allene.²³ To monitor the nuclear motion in the $\tilde{A}^2E/\tilde{B}^2B_2$ electronic manifold of the cation, we construct a model vibronic Hamiltonian⁸ in the dimensionless normal mode coordinates of the ground electronic state (1A_1) of allene pertinent to the D_{2d} symmetry point group. We resort to a diabatic electronic representation³⁴ in which the diverging kinetic coupling terms (of the adiabatic electronic representation) change into smooth potential couplings. That is, in a diabatic electronic representation the elements of the vibronic Hamiltonian are weakly varying functions of the nuclear coordinates and the Condon approximation holds well in the photoexcitation process. In what follows we define Q_i as the dimensionless normal coordinate of neutral allene associated with the vibrational mode ν_i . The vibrational modes $i = 1–3$ are of A_1 symmetry, $i = 4$ is of B_1 symmetry (JT active), $i = 5–7$ are of B_2 symmetry (JT active), and $i = 8–11$ are of E symmetry (PJT active). The nature of each of these modes is described in detail in the literature.^{17,26,35} Following our previous study¹⁷ the Hamiltonian is constructed as follows:

$$H = H_0 \mathbf{1} + \begin{pmatrix} e_{11} & e_{12} & e_{13} \\ e_{21} & e_{22} & e_{23} \\ e_{31} & e_{32} & e_{33} \end{pmatrix} \quad (4)$$

Here $H_0 = \mathcal{T}_N + V_0$, with

$$\mathcal{T}_N = -\frac{1}{2} \sum_{i=1}^7 \omega_i \left[\frac{\partial^2}{\partial Q_i^2} \right] - \frac{1}{2} \sum_{i=8}^{11} \omega_i \left[\frac{\partial^2}{\partial Q_{ix}^2} + \frac{\partial^2}{\partial Q_{iy}^2} \right] \quad (5a)$$

$$V_0 = \frac{1}{2} \sum_{i=1}^7 \omega_i Q_i^2 + \frac{1}{2} \sum_{i=8}^{11} \omega_i (Q_{ix}^2 + Q_{iy}^2) \quad (5b)$$

is the Hamiltonian matrix associated with the electronic ground state of allene and is defined in terms of unperturbed harmonic oscillators with frequencies ω_i . $\mathbf{1}$ is a (3×3) unit matrix. The elements e_{ij} in the above Hamiltonian matrix refer to the interacting (component) states and are expanded in a Taylor series up to second order with respect to the totally symmetric and the JT-active vibrational modes. Using elementary symmetry selection rules the following result is obtained:^{8,15,36}

$$e_{11} = E_E^0 + \sum_{i=1}^3 \kappa_i Q_i + \sum_{i=5}^7 \lambda_i Q_i + \frac{1}{2} \sum_{i=1}^7 \gamma_i Q_i^2 + \sum_{i>j, i,j=1}^3 \Omega_{ij} Q_i Q_j + \sum_{i>j, i,j=5}^7 \Omega_{ij} Q_i Q_j \quad (6a)$$

$$e_{22} = E_E^0 + \sum_{i=1}^3 \kappa_i Q_i - \sum_{i=5}^7 \lambda_i Q_i + \frac{1}{2} \sum_{i=1}^7 \gamma_i Q_i^2 + \sum_{i>j, i,j=1}^3 \Omega_{ij} Q_i Q_j + \sum_{i>j, i,j=5}^7 \Omega_{ij} Q_i Q_j \quad (6b)$$

$$e_{33} = E_{B_2}^0 + \sum_{i=1}^3 \left(\kappa'_i Q_i + \frac{1}{2} \gamma'_i Q_i^2 \right) \quad (6c)$$

$$e_{12} = e_{21} = \lambda_4 Q_4 \quad (6d)$$

$$e_{13} = e_{31} = \sum_{i=8}^{11} \lambda'_i Q_{ix} \quad (6e)$$

$$e_{23} = e_{32} = \sum_{i=8}^{11} \lambda'_i Q_{iy} \quad (6f)$$

The quantities E_E^0 and $E_{B_2}^0$ in the above equations are the vertical ionization energies of the \tilde{A}^2E and \tilde{B}^2B_2 electronic states of $C_3H_4^+$, respectively. κ_i and κ'_i are the linear intrastate coupling constants for the totally symmetric vibrational modes in the \tilde{A}^2E and \tilde{B}^2B_2 electronic states of the ion, respectively. The quantities λ_i and λ'_i denote the linear JT and PJT coupling constants, respectively. The quantities γ_i and γ'_i are the quadratic coupling constants in the \tilde{A}^2E and \tilde{B}^2B_2 electronic states, respectively. Ω_{ij} are the bilinear coupling constants belonging to the A_1 vibronic symmetry ($i, j \leq 3$) or B_2 symmetry ($5 \leq i, j \leq 7$). Higher order couplings are not considered here nor are the mixed A_1-B_2 bilinear terms. The x and y components of the degenerate vibrational modes $\nu_8 - \nu_{11}$ are denoted by Q_{ix} and Q_{iy} , respectively.

The photoelectron spectrum is calculated by Fermi's Golden rule. The photoelectron intensity is given by

$$P(E) = \sum_v |\langle \Psi_v | \hat{T} | \Psi_0 \rangle|^2 \delta(E - E_v + E_0) \quad (7)$$

where $|\Psi_0\rangle$ is the initial vibrational and electronic ground state of allene with energy E_0 . $|\Psi_v\rangle$ is the final $\tilde{A}^2E/\tilde{B}^2B_2$ vibronic state of the allene radical cation and E_v is the vibronic energy. \hat{T} is the transition operator that describes the interaction of the valence $1e$ and $3b_2$ electrons of allene with the external radiation with energy E . The initial and the final states are given by

$$|\Psi_0\rangle = |\Phi^0\rangle |\chi_0^0\rangle \quad (8a)$$

$$|\Psi_v\rangle = |\Phi^{E_x}\rangle |\chi_v^{E_x}\rangle + |\Phi^{E_y}\rangle |\chi_v^{E_y}\rangle + |\Phi^{B_2}\rangle |\chi_v^{B_2}\rangle \quad (8b)$$

where $|\Phi\rangle$ and $|\chi\rangle$ represent the (diabatic) electronic and vibrational part of the wave function, respectively. The superscripts 0, E_x/E_y , and B_2 refer to the 1A_1 electronic ground state of allene, to the x/y components of the \tilde{A}^2E state, and to the \tilde{B}^2B_2 state of the radical cation, respectively. Using eq 8 the excitation function of eq 7 can be rewritten as

$$P(E) = \sum_v |\tau^{E_x} \langle \chi_v^{E_x} | \chi_0^0 \rangle + \tau^{E_y} \langle \chi_v^{E_y} | \chi_0^0 \rangle + \tau^{B_2} \langle \chi_v^{B_2} | \chi_0^0 \rangle|^2 \delta(E - E_v + E_0) \quad (9)$$

with

$$\tau^m = \langle \Phi^m | \hat{T} | \Phi^0 \rangle \quad (10)$$

The quantities τ^m denote the generalized oscillator strengths of the final \tilde{A}^2E and \tilde{B}^2B_2 electronic states of the radical cation.^{8,17} The matrix elements of the transition operator are known to be weakly varying function of the nuclear coordinates and are treated as constants, in accordance with the applicability of the generalized Condon approximation in the diabatic electronic basis.³⁷

The stick vibronic spectrum is calculated numerically by representing the vibronic Hamiltonian H in a direct product basis of harmonic oscillator eigenstates of H_0 . In this basis $|\chi_v^m\rangle$ takes the following form:⁸

$$|\chi_v^m\rangle = \sum_{n_1, n_2, \dots, n_k} a_{v, n_1, n_2, \dots, n_k}^m |n_1\rangle |n_2\rangle \dots |n_k\rangle \quad (11)$$

Here m is the electronic state index, n_l is the quantum number associated with the l th vibrational mode, and k is the total number of such modes. The summation runs over all possible combinations of quantum numbers associated with each mode. For each vibrational mode the oscillator basis is suitably truncated in the numerical calculations. The maximum level of excitation for each mode can be approximately estimated from its coupling strength. The Hamiltonian matrix expressed in a direct product harmonic oscillator basis is highly sparse. Since the final electronic states have different vibronic symmetry the Hamiltonian matrix, in fact, decouples into blocks with E and B_2 symmetry. We tridiagonalize this sparse Hamiltonian matrix by the Lanczos algorithm³⁸ prior to diagonalization. The diagonal elements of the eigenvalue matrix give the position of the vibronic lines and the relative intensities are obtained from the squared first components of the Lanczos eigenvectors.^{8,12}

B. Wave Packet Dynamics: MCTDH Method. The MCTDH method provides an efficient algorithm for the solution of the time-dependent Schrödinger equation. The basis of the method is to use a multiconfigurational ansatz for the wave function, with each configuration expressed as a Hartree product of time-dependent basis functions, known as single-particle functions. The wave packet ansatz appropriate for the nonadiabatic problem studied here is known as the *multiset* formulation:^{31,39}

$$\Psi(q_1, \dots, q_p, t) = \sum_{\alpha=1}^{\sigma} \sum_{j_1=1}^{n_p^{(\alpha)}} \dots \sum_{j_p=1}^{n_p^{(\alpha)}} A_{j_1 \dots j_p}^{(\alpha)}(t) \prod_{\kappa=1}^p \varphi_{j_\kappa}^{(\alpha, \kappa)}(q_\kappa, t) |\alpha\rangle \quad (12)$$

$$= \sum_{\alpha} \sum_J A_J^{(\alpha)} \Phi_J^{(\alpha)} |\alpha\rangle \quad (13)$$

where $\{\alpha\}$ are indices denoting the discrete set of electronic states included in the calculation. Thus, the wave packet, $\Psi^{(\alpha)}$, associated with each electronic state is described using a different set of single-particle functions $\{\varphi_{j_\kappa}^{(\alpha, \kappa)}\}$. Note that the multiindex, $J = j_1 \dots j_p$, depends implicitly on the state α as the maximum number of single-particle functions may differ for different states. The summation \sum_J is shorthand for a summation over all possible index combinations for the relevant state. At this point, the variables for the p sets of single-particle functions are defined only as the "coordinate of a particle". The particle

coordinate may be one-dimensional or multidimensional. Equations of motion for the expansion coefficients, $A_j^{(\alpha)}$, and single-particle functions, $\varphi_{j_k}^{(\alpha,k)}$ have been derived using a variational principle. Full details of the derivation of these equations, their properties, and an efficient integration scheme for their integration are given in ref 30.

The use of a variational principle ensures that the single-particle functions evolve so as to optimally describe the true wave packet; i.e., the time-dependent basis moves with the wave packet. This provides the efficiency of the method by keeping the basis optimally small. Unfortunately, the method suffers from an exponential growth in the computational resources required with the number of particles included in a calculation. This generally restricts a calculation to below 8–10 particles.

The physical system is described by a set of f coordinates, Q_1, \dots, Q_f . In allene, $f = 15$, and so it is impossible to use a set of single-particle functions to describe each vibrational mode. Fortunately, there is no reason a particle coordinate cannot be a set of coordinates, i.e., $q_k = [Q_i, Q_j, \dots]$. The single-particle functions are then multidimensional functions of the set of system coordinates and the number of particles $p < f$. By doing this the computational resources can be significantly reduced, and larger systems can be treated without in any way affecting the variational nature of the method.^{32,33}

To calculate the photoelectron spectrum using a time-dependent formulation, the Fourier transform representation of the delta function is used in the Golden rule formula eqs 7 and 9. This expression can then be reduced to the Fourier transformation of the time autocorrelation function of the wave packet. In the present case the different spatial symmetries of the interacting electronic states result in the presence of a vibronic symmetry; i.e., the vibronic secular matrix becomes block diagonal upon a suitable ordering of basis states. The Golden rule expression is then

$$P(E) \sim \sum_{j=1}^3 |\tau^j|^2 \text{Re} \int_0^\infty e^{iEt/\hbar} C^j(t) dt \quad (14)$$

where $j = 1, 2$ corresponds to the two components (x and y) of the \tilde{A}^2E electronic state and $j = 3$ to the \tilde{B}^2B_2 electronic state. $C^j(t) = \langle \chi^j(t=0) | e^{-iHt/\hbar} \chi^j(t=0) \rangle$ is the time autocorrelation function of the wave packet starting in the electronic state j .

C. Ab Initio Calculations. The details of the ab initio calculations are described in the previous paper.¹⁷ We briefly repeat them here, focusing on the calculation of the higher order coupling constants.

The geometry optimization and the calculations of harmonic vibrational frequencies (ω_i) of allene in its ground electronic state (1A_1) are carried out at the Møller–Plesset perturbation theory (MP2) level employing the correlation-consistent polarized valence triple- ζ (cc-pVTZ) Gaussian basis set of Dunning.⁴⁰ Along with the vibrational frequencies, the transformation matrix from the symmetry coordinates to the mass-weighted normal coordinates is obtained. The dimensionless normal coordinates (Q_i) are obtained by multiplying the latter with $\sqrt{\omega_i}$.¹⁸

The coupling parameters of the Hamiltonian are derivatives of the adiabatic potentials of the cation with respect to the corresponding normal mode coordinates calculated at the equilibrium geometry of the neutral ($\mathbf{Q} = \mathbf{0}$). The linear coupling constants for the \tilde{A}^2E and \tilde{B}^2B_2 electronic states are defined as follows:

$$\kappa_i = \frac{1}{2} \left(\frac{\partial V_E}{\partial Q_i} \right) \bigg|_{Q=0} \quad i = 1-3 \quad (15a)$$

$$\lambda_i = \frac{1}{2} \left(\frac{\partial \Delta V_E}{\partial Q_i} \right) \bigg|_{Q=0} \quad i = 4-7 \quad (15b)$$

Here $2\Delta V_E$ is the (signed) difference of the JT split potential energy surfaces of the \tilde{A}^2E state, and care has to be taken that symmetry-adapted potential energy functions are used to calculate it in order to avoid the discontinuous behavior of the adiabatic potential energy functions at $\mathbf{Q} = \mathbf{0}$. An expression analogous to eq 15a holds for κ'_i . The interstate coupling constants for the degenerate vibrational modes are given by

$$\lambda'_i = \frac{1}{2} \sqrt{\left| \left(\frac{\partial^2 \Delta V_E}{\partial Q_i^2} \right) \right|_{Q=0}} \quad i = 8-11 \quad (16)$$

Here $\Delta E = \Delta V_{Q_i}^2 - \Delta V_0^2$, where ΔV_{Q_i} and ΔV_0 are the potential energy differences between the \tilde{B}^2B_2 and \tilde{A}^2E ionic states for the normal mode displacement Q_i , and at the equilibrium geometry ($\mathbf{Q} = \mathbf{0}$), respectively. The second order and the bilinear coupling constants, which constitute essential ingredients of the present work, are similarly given by

$$\gamma_i = \left(\frac{\partial^2 V_E}{\partial Q_i^2} \right) \bigg|_{Q=0} \quad i = 1-7 \quad (17a)$$

$$\Omega_{ij} = \left(\frac{\partial^2 V_E}{\partial Q_i \partial Q_j} \right) \bigg|_{Q=0} \quad i \neq j \quad (17b)$$

The above coupling constants are determined by calculating vertical ionization energies of allene by the outer valence Green's function method, again employing the cc-pVTZ basis set. The electronic structure calculations were performed for a series of displacements (from the MP2 equilibrium geometry at $\mathbf{Q} = \mathbf{0}$) along the dimensionless normal coordinate $Q_i = 0.5$ and 1.0 using the GAUSSIAN program package.²⁸ The energy derivatives appearing in eqs 16–18 are then approximated by a suitable finite difference formula. The resulting coupling constants for the \tilde{A}^2E and the \tilde{B}^2B_2 electronic states are listed in Table 1 and 2. We note that the linear coupling constants differ slightly from those noted in the previous article¹⁷ because of the use of a more accurate (i.e., symmetric) finite difference formula.

III. Results and Discussion

A. Photoelectron Spectrum. The full composite photoelectron band for the $\tilde{A}^2E/\tilde{B}^2B_2$ electronic states of $C_3H_4^+$ is obtained by the wave packet propagation approach within the MCTDH scheme. All 15 normal vibrational modes are considered in the calculation. The parameters of the Hamiltonian are those reported in Tables 1 and 2.

The first step in setting up an MCTDH calculation is to choose a set of primitive basis functions in which the single-particle functions, their time derivatives, and the Hamiltonian can be represented at each point in time along the propagation path. For large systems, such as that studied here, a combination scheme for the degrees of freedom must then be selected to reduce the computational resources required for a calculation. Finally, a set of single-particle functions must be specified in which the evolving wave packet is accurately represented. Table 3 summarizes the choices made for the description of the allene system.

TABLE 1: Ab Initio Calculated Linear and Quadratic Coupling Constants for the \tilde{A}^2E and \tilde{B}^2B_2 States^a of the Allene Radical Cation ($C_3H_4^+$) and the Vibrational Frequencies of Allene in Its Electronic Ground (1A_1) State^b

mode	κ or λ \tilde{A}^2E	κ' \tilde{B}^2B_2	λ' $\tilde{A}^2E \otimes \tilde{B}^2B_2$	γ \tilde{A}^2E	γ' \tilde{B}^2B_2	ω expt ³⁵	ω
ν_1 (A_1)	-0.288	-0.164		0.282	0.011	0.3945	0.3738
ν_2 (A_1)	-0.251	0.450		-0.060 ^c	0.018	0.1846	0.1789
ν_3 (A_1)	-0.209	0.00002		0.0035	0.013	0.1359	0.1330
ν_4 (B_1)	0.103			-0.045		0.1110	0.1072
ν_5 (B_2)	0.276			0.280		0.3944	0.4224
ν_6 (B_2)	0.114			0.0055		0.2529	0.2426
ν_7 (B_2)	0.334			-0.065 ^c		0.1782	0.1733
ν_8 (E)			0.245			0.4055	0.4322
ν_9 (E)			0.237			0.1260	0.1238
ν_{10} (E)			0.133			0.1069	0.1043
ν_{11} (E)			0.044			0.0446	0.0440

^aAb initio value of the vertical energy gap between the \tilde{A}^2E and \tilde{B}^2B_2 electronic states is 0.21 eV. ^bAll quantities are in eV if not otherwise stated. The theoretical (experimental) results represent the harmonic (fundamental) vibrational frequencies. ^cAdjusted value -0.02 eV.

TABLE 2: Ab Initio Calculated Bilinear Coupling Constants (eV) for the \tilde{A}^2E Electronic Manifold of the Allene Radical Cation ($C_3H_4^+$)

modes i, j	Ω_{ij}
ν_1, ν_2	0.043 ^a
ν_1, ν_3	0.0042
ν_2, ν_3	-0.022 ^b
ν_5, ν_6	0.004
ν_5, ν_7	0.043 ^a
ν_6, ν_7	0.0185

^aAdjusted value 0.025 eV. ^bAdjusted value -0.03 eV.

TABLE 3: Details of the Basis Functions Used To Describe the Particles in the MCTDH Calculations^a

particle	normal modes	primitive basis ^b	SPF basis [E_x, E_y, B_2] ^c	
			Initial E_y ^d	Initial B_2 ^e
1	(ν_1, ν_4, ν_6)	(10, 14, 10)	[6, 6, 6]	[7, 7, 6]
2	(ν_2, ν_3)	(32, 24)	[9, 10, 8]	[12, 12, 8]
3	($\nu_{10x}, \nu_{10y}, \nu_{11x}$)	(12, 12, 8)	[6, 6, 6]	[9, 9, 8]
4	(ν_5, ν_7)	(10, 30)	[8, 8, 6]	[8, 8, 7]
5	($\nu_{8x}, \nu_{8y}, \nu_{11y}$)	(10, 10, 8)	[6, 7, 6]	[7, 7, 8]
6	(ν_{9x}, ν_{9y})	(18, 18)	[6, 7, 6]	[10, 10, 9]

^aThe calculations were converged with respect to the spectrum. Vibrational modes bracketed together were treated as a single particle, e.g., particle 1 is a 3-dimensional particle including modes ν_1, ν_4 , and ν_6 . The primitive basis is the number of Harmonic oscillator DVR functions, in the dimensionless coordinate system, required to represent the system dynamics along the relevant mode. The SPF basis is the number of single-particle functions used, one set for each of the three electronic states. Different numbers of functions were required depending on whether the initial wave packet was in the E_y or B_2 state. ^bThe primitive basis for each particle is the product of the one-dimensional bases; e.g., for particle 1 the primitive basis was $10 \times 14 \times 10 = 1400$ functions. The full primitive basis consists of a total of 9.63×10^{16} functions. ^cCalculations starting in the E_y and B_2 state are listed separately. E.g., starting in the E_y state particle 1 required 6 functions in each state. ^dThere are 296 640 configurations altogether and the run required 7.5 h and 95 MB on a DEC 500au workstation. ^eThere are 1 040 256 configurations altogether and the run required 30 h and 243 MB on a DEC 500au workstation.

The primitive basis chosen is a harmonic oscillator discrete variable representation (DVR) (see, for example, Appendix B in ref 30 for more details of this basis). The 15 vibrational modes are combined into 6 particles, so that the product primitive grid required for each particle remains a reasonable size. The combinations used are given in Table 3. For example, the first particle contains three degrees of freedom, the ν_1, ν_4 , and ν_6 vibrational modes. The primitive basis set for this particle is thus $12 \times 8 \times 8 = 768$ functions. The initial single-particle functions are sets of ortho-normalized harmonic oscillator functions in the mass-frequency scaled coordinate system used.

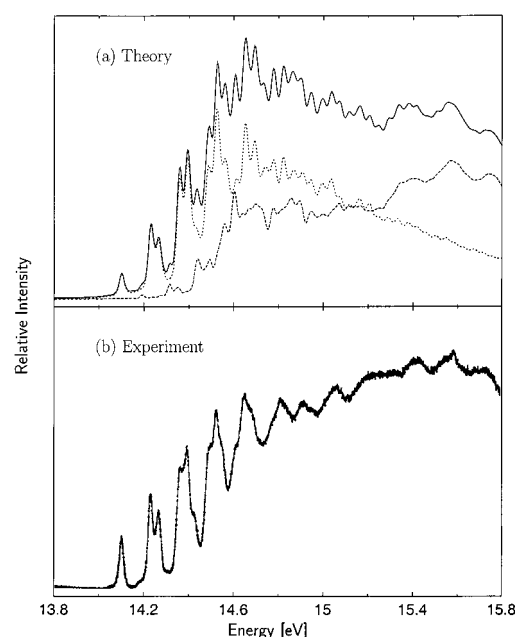


Figure 1. Photoelectron spectrum for the $\tilde{A}^2E/\tilde{B}^2B_2$ electronic manifold of $C_3H_4^+$. The intensity (in arbitrary units) is plotted as a function of the energy of the final vibronic states. (a) Results obtained by the wave packet propagation method within the MCTDH scheme considering all 15 vibrational degrees of freedom. The full photoelectron band is shown by the solid line and the contributions of E and B_2 vibronic symmetries are shown by the dotted and dashed lines, respectively. (b) The 21.218 eV He I excited experimental recording of Baltzer et al., reproduced from ref 23.

In the multiset formalism, one set is required for each particle for each electronic state. The initial wave function is the ground state vibrational eigenfunction, which is simply a product of the first single-particle functions in each set. The primitive basis used means that the initial wave function for the propagations is exactly represented.

The sizes of both the primitive and single-particle function bases are selected so that the calculations are converged with respect to the spectrum; i.e., the calculated spectrum does not change on adding functions.

The photoelectron band thus obtained is shown in Figure 1 (panel a) along with the high-resolution He I excited experimental recording of Baltzer et al.²³ (panel b). The theoretical spectrum is a sum of contributions from the three states. From eq 14, each contribution is the Fourier transform of the autocorrelation function $C^j(t)$ computed with an initial wave packet located on the j th electronic state. In Figure 1a the full theoretical spectrum is shown by the solid line and the

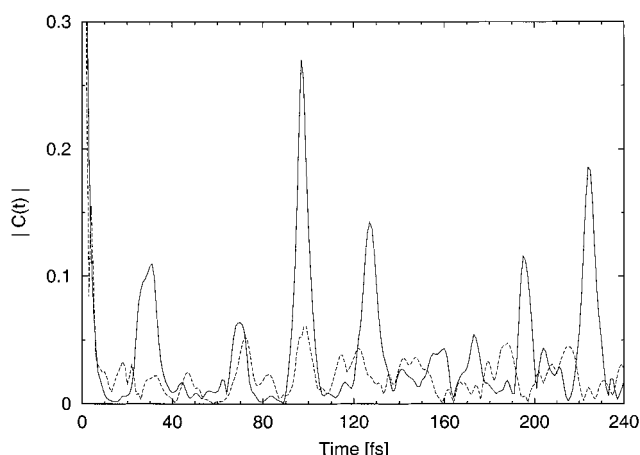


Figure 2. Absolute value of the time autocorrelation function $|C(t)|$ of the \tilde{A}^2E electronic manifold (solid line) and the \tilde{B}^2B_2 electronic state (dashed line) of the allene radical cation. $C(t)$ is computed by locating the initial wave packet separately on the respective electronic state.

contributions from the E and B_2 vibronic symmetries are plotted separately and are shown by the dotted and the dashed lines, respectively. We have used a value $|\tau^E/\tau^{B_2}| = 1/2$ in the full spectrum in order to better reproduce the relative height of the envelopes for the \tilde{A}^2E and \tilde{B}^2B_2 ionic states. The vertical energy gap between the \tilde{A}^2E and \tilde{B}^2B_2 ionic states is fixed at 0.43 eV, which is close to the value we obtained from the ab initio calculations (cf. Table 1). The vertical ionization potentials, $E_E^0 = 14.93$ eV and $E_{B_2}^0 = 15.36$ eV, are used, which reproduce the origin of the photoelectron band at the experimentally observed energy at 14.1 eV.

To calculate the above spectrum, the wave packet is propagated for 120 fs. Since we start with a real initial wave packet, we can use the relationship $C(2t) = \langle \Psi^*(t) | \Psi(t) \rangle$, which allows an increase of the energy resolution ($\Delta E = 2\pi\hbar/T$) in the photoelectron spectrum by a factor of 2 by effectively doubling the total propagation time T .⁴¹ The resulting $C(t)$ up to time $T = 240$ fs is plotted in Figure 2. The dashed and the solid curves are obtained from two separate calculations by locating an initial wave packet on one of the components of the \tilde{A}^2E and on the \tilde{B}^2B_2 electronic state, respectively. It can be seen that $C(t)$ of the \tilde{A}^2E electronic manifold exhibits a regular recurrence pattern. On the other hand, $C(t)$ of the \tilde{B}^2B_2 electronic state is quite irregular and decays much faster than that of the \tilde{A}^2E electronic manifold. This behavior is manifested in the photoelectron spectrum in Figure 1a, which reveals a sharp progression of spectral peaks at low energies due to the JT activity in the \tilde{A}^2E electronic manifold, and a highly diffuse structure (relating to the faster decay of $C(t)$) at high energies due to the PJT interactions of this manifold with the \tilde{B}^2B_2 electronic state.

In an experimental spectrum the lines are broadened due to the resolution of the spectrometer. This effect can be added to the calculated spectra by convoluting the spectral lines with a suitable peaked curve, which in the time-dependent picture is equivalent to damping the autocorrelation function by a time-dependent function. By a careful choice of the function, effects due to the finite length of the propagation can be eliminated. For example, the function³⁰

$$F(t) = \cos\left(\frac{\pi t}{2T}\right) \quad (18)$$

is taken in the present case, with T the length of the time propagation. As $t \rightarrow T$, $F(t)C(t) \rightarrow 0$, therefore, the artifacts in

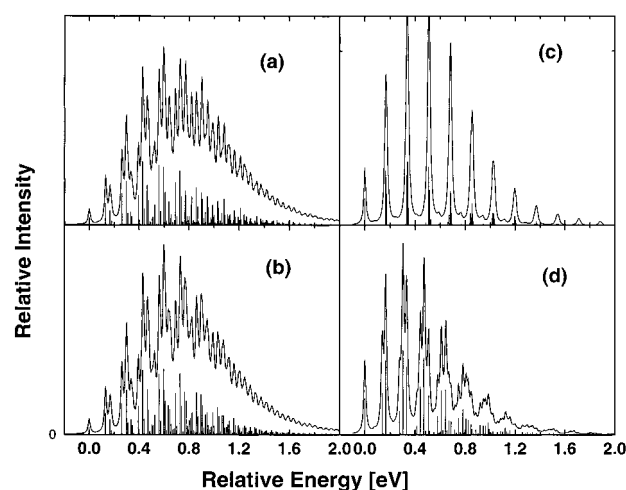


Figure 3. Vibronic spectra for the \tilde{A}^2E electronic states of the allene radical cation ($C_3H_4^+$) in the absence of PJT coupling. Stick spectra are obtained by considering the (a) v_2 , v_3 , v_4 , v_5 , and v_7 , (b) v_2 , v_3 , v_5 , and v_7 , (c) v_2 , v_4 , v_5 , and v_7 , and (d) v_3 , v_4 , v_5 , and v_7 vibrational modes in the calculations (see text for further details). The stick vibronic spectrum in each panel is convoluted with a Lorentzian function with fwhm 10 meV to generate the spectral envelope.

the spectrum due to finite time Fourier transformation are reduced. Multiplying $C(t)$ with $F(t)$ is equivalent to convoluting the spectrum with the Fourier transform of $F(t)$, which in this case reads³⁰

$$\tilde{F}(E) = \frac{4\pi T}{\pi^2 - (2ET)^2} \cos(ET) \quad (19)$$

with a full width at half-maximum (fwhm) of $\Gamma = 3.4/T$ (fs) (here $\Gamma = 14$ meV). Further phenomenological broadening, due to the spectral resolution and neglect of the interaction with an external heat bath, is added by the function

$$G(t) = \exp\left(-\frac{t}{\tau_r}\right) \quad (20)$$

with τ_r being the relaxation of the system. This leads to a Lorentzian broadening of the spectrum with $\Gamma = 2/\tau_r$. In Figure 1a the spectra of E and B_2 vibronic symmetries are obtained by damping the respective autocorrelation functions with $\tau_r = 50$ fs (i.e., here $\Gamma = 26$ meV).

To clearly identify the progression of peaks in the above photoelectron band at low energies and the impact of higher order couplings on them, we carried out companion calculations and systematically analyzed the “stick” vibronic spectrum of the \tilde{A}^2E electronic manifold (without the PJT coupling with the \tilde{B}^2B_2 state). The stick vibronic spectra thus obtained are presented in Figure 3a–d (as a function of vibronic energies relative to the ground state of neutral allene) along with the spectral envelope obtained by convoluting the corresponding stick spectrum with a Lorentzian function with fwhm of 10 meV. The spectrum in Figure 3a is obtained by considering five vibrational modes v_2 , v_3 , v_4 , v_5 , and v_7 in the dynamical treatment. We have used 25, 25, 15, 15, and 25 harmonic oscillator basis functions for the above modes in that order. This choice leads to a secular matrix of dimension 7031250 pertinent to the two-state matrix Hamiltonian within the \tilde{A}^2E electronic manifold. This Hamiltonian matrix is then tridiagonalized using 3000 Lanczos iteration steps to obtain the stick spectrum (see also section II.A above). The convergence of the latter is explicitly checked by altering the number of basis functions as

well as the number of Lanczos iteration steps. In this way it has been ensured that the stick spectrum and the spectral envelope are converged to within drawing accuracy. The coupling parameters of the Hamiltonian are those reported in Tables 1 and 2. The spectrum of Figure 3a compares well with the low-energy part of the full composite band presented in Figure 1a. The fine structure of the two envelopes are identical, from which it can be concluded that PJT couplings are not important for the progression of peaks at low energies.

Two different progressions are clearly visible in the spectrum in Figure 3a. They are ~ 0.13 and ~ 0.16 – 0.17 eV apart. Energetically they are close to the frequencies of the ν_3 , ν_7 , and ν_2 vibrational modes, which are 0.136, 0.178, and 0.185 eV, respectively, in the neutral ground state (cf. Tables 1 and 2). Therefore, the observed line spacings must correspond to the above frequencies in the neutral allene altered by the Duschinsky rotation of the normal modes⁴² (an amount nearly equal to the quadratic coupling constants) in the cationic \tilde{A}^2E electronic manifold. In their experimental work, Yang et al.²² assigned the above progressions to the symmetric vibrational modes ν_3 and ν_2 . In a theoretical work, Woywod and Domcke²⁶ have re-assigned these progressions to be due to the JT-active mode ν_7 and the symmetric mode ν_2 . Subsequently, the experimental work of Baltzer et al.²³ and our previous theoretical work¹⁷ followed the assignments of Woywod and Domcke.²⁶ However, the present more elaborate investigation reveals that these progressions are due to the symmetric mode ν_3 and a combination of modes ν_2 and ν_7 . This aspect is further discussed below.

In Figure 3b we show the above spectrum calculated without including the JT-active torsional mode ν_4 (B_1). It can be seen by comparing with Figure 3a that the torsional mode does *not* contribute to the progression of spectral lines at low energies. This mode is only moderately excited at higher energies and thus contributes to the diffuseness of the spectral envelope at those energies. The spectrum obtained by considering the vibrational modes ν_2 , ν_4 , ν_5 , and ν_7 is shown in Figure 3c. Without the mode ν_3 , the characteristic structures in the photoelectron band disappear and the spectral progression dramatically changes, almost to a single mode progression. The progression in Figure 3c clearly confirms that the ν_2 and ν_7 vibrational modes combine together to form a single progression in the full spectrum. The spectrum in Figure 3c is to be compared with the one resulting from a linear coupling model considering the same vibrational modes and shown in our earlier paper (see Figure 5b in ref 17). The difference in the two spectra clearly shows the importance of the higher order coupling terms employed in the present investigation. The spectrum calculated by considering vibrational modes ν_3 , ν_4 , ν_5 , and ν_7 is shown in Figure 3d. It is clearly revealed by Figure 3d that the vibrational modes ν_3 and ν_7 form two distinct progressions. We note that the bilinear coupling constant Ω_{23} is set to zero in the calculations of the spectra shown in Figure 3c,d. In comparison with Figure 3a one can see that Ω_{23} redistributes the spectral intensity between ν_2 and ν_3 significantly. We note that the vibrational mode ν_5 plays no significant role in the low-energy progression. It can also be seen from Table 1 that the excitation strength ($\kappa_5^2/2\omega_5^2$) of this mode is quite small. However, we retain this mode in the present analysis in order to be consistent with our earlier study.

Although the overall appearance of the composite photoelectron band of the $\tilde{A}^2E/\tilde{B}^2B_2$ electronic manifold of $C_3H_4^+$ presented in Figure 7 of ref 17 looks similar to the full 15-mode results in Figure 1a above, there are some distinct

differences between them. In particular, the spectral intensity at high energies improved on considering all 15 vibrational modes. The rather prominent dip in the envelope in the ~ 14.8 – 15.5 eV energy range becomes more shallow in the present simulation and compares better with the experimental results. Also in our previous study¹⁷ we employed a LVC scheme and we had to adjust the vibrational frequencies and coupling constants of ν_2 and ν_7 vibrational modes to a large extent in order to obtain a reasonable agreement with the experimental recording. The vertical energy gap between the \tilde{A}^2E and \tilde{B}^2B_2 states (cf. Table 1) was adjusted to 0.65 eV. In contrast to these, in the present investigation results are obtained by adjusting only a few higher order coupling constants (see Tables 1 and 2). The vertical energy gap is also adjusted to a lesser extent to 0.43 eV. Finally, the physics underlying the resolved line structures at low energies is different (as stated above) in the two studies.

The above findings on the \tilde{A}^2E and \tilde{B}^2B_2 band are further complemented by investigating the geometry change of allene on photoexcitation. First we focus on the LVC model and calculate the geometry change in internal coordinates in the subspace of the A_1 and B_2 vibrational modes. The transformation matrix from the dimensionless normal coordinate to the internal coordinate is obtained by the GF matrix method of Wilson et al.¹⁸ Without the PJT coupling the adiabatic potential energies of the \tilde{A}^2E electronic manifold can be obtained from the $E\otimes B$ JT part of the electronic Hamiltonian in eq 4:

$$H_{el}^{JT} = V_0 \mathbf{1} + \begin{pmatrix} E_E^0 + \sum_{i=1}^3 \kappa_i Q_i + \sum_{i=5}^7 \lambda_i Q_i & \lambda_4 Q_4 \\ \lambda_4 Q_4 & E_E^0 + \sum_{i=1}^3 \kappa_i Q_i - \sum_{i=5}^7 \lambda_i Q_i \end{pmatrix} \quad (21)$$

where $V_0 = \sum_{i=1}^7 \omega_i Q_i^2/2$ and $\mathbf{1}$ is a (2×2) unit matrix. The eigenvalues of the above Hamiltonian are given by^{8,17,43}

$$V_{\mp}(\mathbf{Q}) = V_0(\mathbf{Q}) + E_E^0 + \sum_{i=1}^3 \kappa_i Q_i \mp \sqrt{\left(\sum_{i=5}^7 \lambda_i Q_i\right)^2 + \lambda_4^2 Q_4^2} \quad (22)$$

where \mp refer to the two adiabatic sheets. Since the results discussed below reveal no torsional displacements at equilibrium (as well as no PJT displacements, which justifies the use of the Hamiltonian, eq 21, we can as well use the diagonal elements of H_{el}^{JT} rather than the surfaces of eq 22. The former correspond to E component states of B_1 and B_2 symmetry in the appropriate C_{2v} subgroup, which is attained when displacing the molecule along a B_2 mode normal coordinate (of the D_{2d} point group). Since the B_2 mode displacements have the effect of removing the symmetry of the left (L) and right (R) terminal CH_2 groups, the overall distortion results in different structural parameters for these moieties. With the linear coupling constants and the vibrational frequencies noted in Table 1 one obtains $\beta(HCC) = 136.4^\circ$, $r(C-H) = 1.01$ Å, and $R(C-C) = 1.35$ Å for the L terminal and $\beta = 119.5^\circ$, $r = 1.06$ Å, and $R = 1.32$ Å for the R terminal of the allene radical cation in the \tilde{A}^2E electronic manifold. The ground-state equilibrium geometry of neutral allene corresponds to $\beta = 120.82^\circ$, $r = 1.08$ Å, and $R = 1.31$ Å.¹⁷ Therefore, one can see that in the photoionization

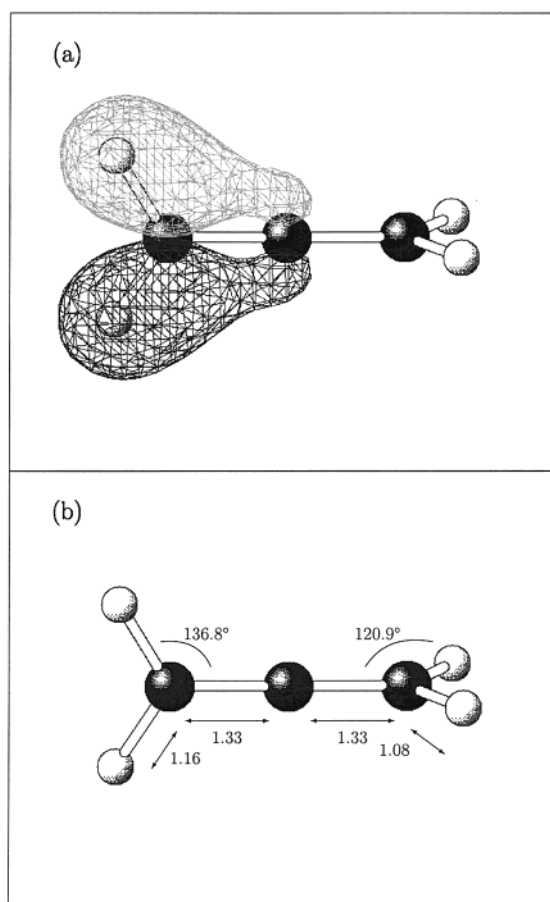


Figure 4. (a) Orbital diagram for one 1e component of $C_3H_4^+$ indicating its highly localized nature and (b) the CASSCF optimized geometry for the \tilde{A}^2E electronic manifold of $C_3H_4^+$. Bond lengths are given in Å.

process mostly one terminal of the molecule is involved (here called the L terminal). In Figure 4a the orbital diagram for one 1e component of $C_3H_4^+$ is shown. The photoelectron spectrum results on ionizing an electron from this orbital. The highly localized nature of this orbital immediately makes clear that also the structural change is mostly localized on that terminal. Of course, there is another 1e component orbital with L and R term interchanged. The same holds then for the corresponding geometry change. The above estimates are only approximate, relying solely on the LVC model. We have further confirmed this localization by optimizing the geometry for the \tilde{A}^2E electronic manifold of $C_3H_4^+$. We have carried out CASSCF calculations for the open-shell system by employing a double- ζ basis set with polarization functions (DZP) on all atoms. The CAS consists of seven electrons and eight valence orbitals. Four of these orbitals are of B_1 symmetry and another four are of B_2 symmetry. The resulting optimized geometry is indicated in Figure 4b. It can be seen that the optimized geometry corresponds closely to the estimates given above. The deviations are somewhat larger for the C–H bond distances.

The present finding of a highly localized distortion bears some similarity to the phenomenon of “dynamic core–hole localization” identified by us for systems with several equivalent core–hole sites.^{44,45} In the latter case there is no degeneracy by symmetry but rather a near-degeneracy of various symmetry adapted core–hole states if the nuclear centers are significantly far apart in space. This holds true, for example, for the C 1s core–hole states of ethylene⁴⁴ or the O 1s core–hole states of CO_2 .⁴⁵ For an asymmetric distortion that destroys the formal

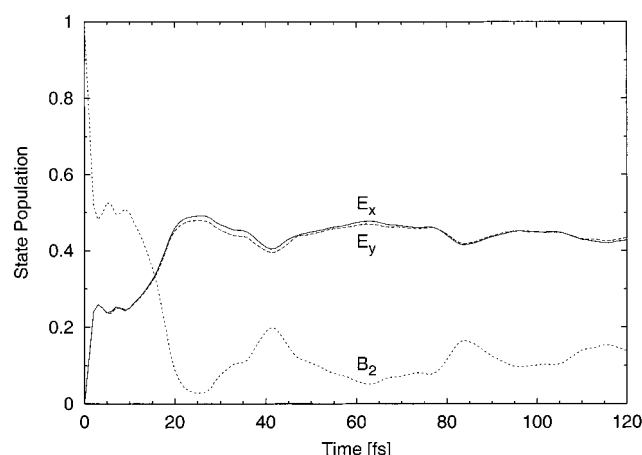


Figure 5. Time evolution of the diabatic electronic populations obtained by locating an initial wave packet on the \tilde{B}^2B_2 electronic state of $C_3H_4^+$. The decay of the population of the \tilde{B}^2B_2 electronic state is shown by the dotted line and the growth of the populations of the two components of the \tilde{A}^2E electronic manifold is shown by the solid and dashed lines, respectively.

equivalence of the core–hole sites the core–holes quickly become localized, which in turn enables a distortion at equilibrium that is mostly localized on one of the core–hole sites.⁴⁴ In terms of delocalized (symmetry-adapted) vibrational modes this gives rise to excitation of near-degenerate pairs of modes that represent symmetrical and antisymmetrical contributions of localized geometry changes. This is just what we find in Figure 3c for the modes ν_2 and ν_7 . Their normal coordinates mostly represent symmetric and antisymmetric combinations of HCH angle changes at both CH_2 moieties. Remember, that it is mostly the CH_2 angle that undergoes a (localized) change according to our above analysis. Thus, structural findings and those on spectral line structures confirm each other in a consistent manner. We mention in passing that the 2e orbital of allene is similarly localized on either of the $C=C$ double bonds so that a similarly localized equilibrium structure of the \tilde{X}^2E ground state of the radical cation can be expected.

B. Time-Dependent Dynamics. We now discuss the femtosecond internal conversion dynamics of $C_3H_4^+$ driven by the nonadiabatic interactions. In Figure 5 the time evolution of the \tilde{A}^2E and \tilde{B}^2B_2 diabatic electronic populations are shown. The wave packet is initially located on the \tilde{B}^2B_2 electronic state and the population decay of this state is shown by the dotted line. The growth of the \tilde{A}^2E electronic populations (of the x and y components) are shown by the solid and the dashed lines. Their difference (which should be zero) is a measure for the convergence of the calculations, which has not been fully achieved for this property. However, since the error is small we can neglect it for our present purposes. It can be seen from Figure 5 that $\sim 75\%$ of the \tilde{B}^2B_2 state population decays within 5 fs. The population of this state becomes almost zero within 20 fs. This initial fast decay of the population relates to a decay rate of ~ 10 fs of the \tilde{B}^2B_2 electronic state and is due to the PJT coupling with the \tilde{A}^2E electronic manifold via the degenerate vibrational modes. At longer times a beat structure appears in the \tilde{B}^2B_2 population curve, which is due to the recrossing of the wave packet from the \tilde{A}^2E to the \tilde{B}^2B_2 electronic state.

To understand the above population dynamics in a better way, in Figure 6a–f we show snapshots of the wave packet evolving in the $\tilde{A}^2E/\tilde{B}^2B_2$ electronic manifold. The probability density of the wave packet is superimposed on the potential energy curves along the normal coordinate of the vibrational mode ν_2 . The potential energy curves and the wave packet probability

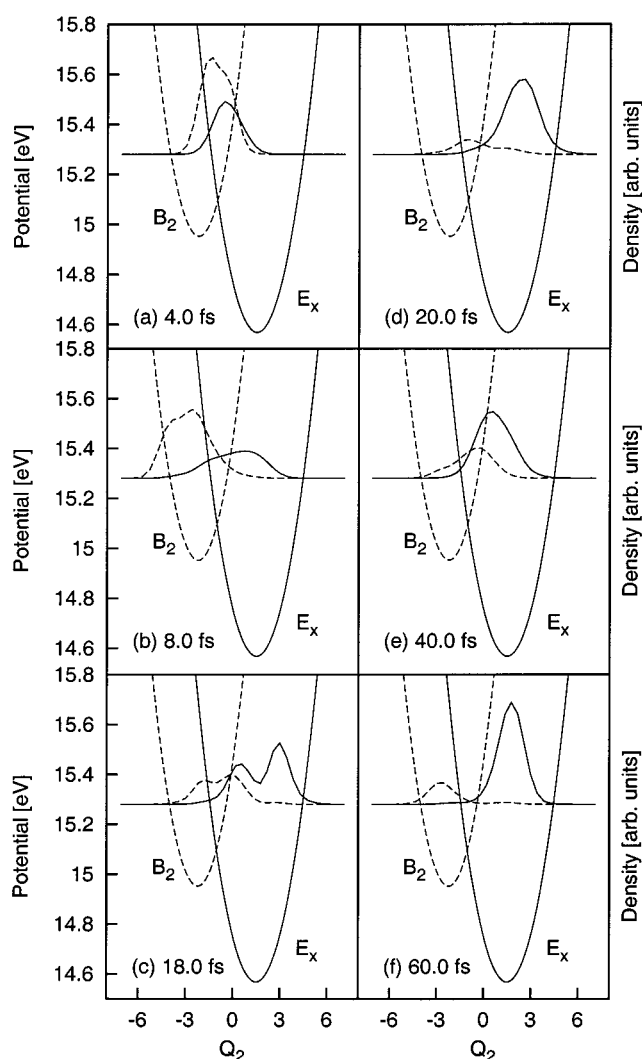


Figure 6. Probability densities ($|\Psi|^2$) as a function of Q_2 integrated over all other coordinates of the wave packet at different times (indicated in each panel) superimposed on the Q_2 potential energy curves (parabolas) of the \tilde{A}^2E and \tilde{B}^2B_2 electronic states of $C_3H_4^+$. Only the density for one component of the \tilde{A}^2E electronic manifold is plotted, and the solid and dashed lines refer to the \tilde{A}^2E and \tilde{B}^2B_2 electronic states, respectively. The zero of the density has been chosen, for graphical reasons, to occur near a potential energy of 15.28 eV. The scale for the probability density is arbitrary but identical for all $|\Psi|^2$ displayed in the figure.

densities are shown as dashed and solid lines for the \tilde{A}^2E and the \tilde{B}^2B_2 electronic states, respectively. The zero of the probability densities is chosen, for graphical reasons, to occur near a potential energy of 15.28 eV. The vibrational mode ν_2 is the strongest Condon active mode (cf. Table 1) and most of the structures in the population diagram in Figure 5 can be understood from the snapshots of the wave packet along this mode. While the two components of the \tilde{A}^2E electronic manifold remain degenerate, a crossing of this manifold with the \tilde{B}^2B_2 electronic state occurs along Q_2 . Because of the different signs of the linear coupling constants κ_2 and κ'_2 , the minima of the two electronic states are on opposite sides of the point of crossing. Initially, the wave packet (not shown in the figure) is located on the \tilde{B}^2B_2 electronic state, and therefore, the population of this state starts from unity. In about 4 fs a considerable population transfer occurs to the \tilde{A}^2E electronic manifold (see Figure 6a), which leads to the sharp decrease of \tilde{B}^2B_2 electronic population in Figure 5 within this time. In about 8 fs (Figure 6b) the wave packet components on the two states move away

from the crossing point and in opposite directions (toward the minimum of the respective potential energy curves). The interference of the wave packet components in the vicinity of the curve crossing leads to the appearance of structures in the population diagram around that time. At longer time the wave packet component on the \tilde{B}^2B_2 electronic state again moves toward the point of crossing, and in about 18–20 fs (Figure 6c,d) much of the wave packet goes over to the \tilde{A}^2E electronic manifold and thus the \tilde{B}^2B_2 electronic population decreases almost to zero. At longer times of ~ 40 fs, the wave packet component of the \tilde{A}^2E electronic manifold moves back toward the crossing point and a fraction of it recrosses to the \tilde{B}^2B_2 electronic state (Figure 6e). This leads to the appearance of the beat structure in the \tilde{B}^2B_2 electronic population diagram around that time (see Figure 5). At still longer times of ~ 60 fs, the wave packet component on the \tilde{B}^2B_2 state again goes over to the \tilde{A}^2E electronic manifold and this process of transfer of the wave packet components back and forth between the two electronic states continues until the end of the time evolution considered.

IV. Summary and Conclusions

We have presented the results of our theoretical investigations on the valence excited photoelectron spectrum of allene pertinent to the $\tilde{A}^2E/\tilde{B}^2B_2$ electronic manifold of the allene radical cation. We employed a second-order vibronic Hamiltonian in the calculations and have shown that the results differ considerably from the ones obtained with a linear vibronic coupling scheme. Ab initio calculations were carried out in order to determine the coupling constants of the Hamiltonian and the optimized geometries of the excited states of the radical cation. The full photoelectron band was calculated by a wave packet propagation technique within the MCTDH scheme considering all fifteen vibrational degrees of freedom. Our results are in good agreement with the high-resolution experimental recording of Baltzer et al.²³ The structures in the photoelectron band are carefully analyzed through companion calculations of the stick vibronic spectra in reduced dimensions. The time-dependent dynamics is further illustrated in terms of time evolution of the diabatic electronic populations as well as nuclear probability densities. The photoelectron band exhibits regular progressions of peaks at low energy and a highly diffused structure at high energies. In our previous study, following Woywod and Domcke²⁶ we confirmed that the structures at low energies originate solely due to the $E\otimes B$ JT activity within the \tilde{A}^2E electronic manifold. However, we found that the highly diffuse structure at high energies originates mainly from PJT type of interactions of this electronic manifold with the next higher \tilde{B}^2B_2 electronic state. Following earlier theoretical work we assigned the low-energy spectral progressions to the ν_2 and ν_7 vibrational modes. In contrast, Yang et al., in their experimental work proposed these progressions to be due to the ν_2 and ν_3 vibrational modes. In this present work we have resolved this discrepancy and found that the low-energy progressions are formed by the vibrational mode ν_3 and a combination of modes ν_2 and ν_7 .

The combined excitation of ν_2 and ν_7 has been related to a localized geometry change in the \tilde{A}^2E state of $C_3H_4^+$, i.e., affecting only one of the C–CH₂ terminal groups. This new finding is related to the phenomena of dynamical core–hole localization identified by us earlier for quite different systems. It has been corroborated by unconstrained geometry optimization and can be understood by inspecting the nodal properties of the pertinent molecular orbital. The agreement between the structural data predicted by the PJT model and those resulting

from the unconstrained geometry optimization provides a test for the validity of the PJT model which underlies the dynamical calculations.

The time evolution of the diabatic electronic populations reveals a nonradiative decay time of ~ 10 fs of the \tilde{B}^2B_2 electronic state of the allene radical cation mediated by the PJT interaction with the \tilde{A}^2E electronic manifold through the degenerate vibrational modes. The transformation of the wave packet components through the $\tilde{A}^2E/\tilde{B}^2B_2$ crossing seam is analyzed to shed further light on the population dynamics. The $\tilde{A}^2E/\tilde{B}^2B_2$ photoelectron band of allene radical cation represents a unique and complex example of the interplay between the JT and PJT type of interactions, with nondegenerate vibrational modes involved in the JT activity. The detailed theoretical investigations presented here, therefore, adds to the understanding of such interactions in molecular dynamics.

Acknowledgment. This study is financially supported by the Deutsche Forschungsgemeinschaft and the Volkswagen Stiftung (G.A.W. and L.S.C.). S.M. gratefully acknowledges a research fellowship from the Department of Science and Technology, New Delhi, under the young scientists scheme. We thank Dr. Thomas Sommerfeld for providing us with the CASSCF results on the \tilde{A}^2E electronic manifold of $C_3H_4^+$.

References and Notes

- Turner, D. W.; Baker, C.; Baker, A. D.; Brundle, C. R. *Molecular Photoelectron Spectroscopy*; Wiley: New York, 1970.
- Neumark, D. M. *Acc. Chem. Res.* **1993**, *26*, 33.
- Polanyi, J. C.; Zewail, A. H. *Acc. Chem. Res.* **1995**, *28*, 119.
- Held, A.; Schlag, E. W. *Acc. Chem. Res.* **1998**, *31*, 467.
- Wenthold, P. G.; Lineberger, W. C. *Acc. Chem. Res.* **1999**, *32*, 597.
- Faraday Discuss.* **2000**, *115*, 1–.
- Teller, E. *J. Phys. Chem.* **1937**, *41*, 109. Herzberg, G.; Longuet-Higgins, H. C. *Discuss. Faraday Soc.* **1963**, *35*, 77. Carrington, T. *Discuss. Faraday Soc.* **1972**, *53*, 27; *Acc. Chem. Res.* **1974**, *7*, 20. Davidson, E. R. *J. Am. Chem. Soc.* **1977**, *99*, 397.
- Köppel, H.; Domcke, W.; Cederbaum, L. S. *Adv. Chem. Phys.* **1984**, *57*, 59.
- Bernardi, F.; Olivucci, M.; Robb, M. *Chem. Soc. Rev.* **1996**, *25*, 321.
- Domcke, W.; Stock, G. *Adv. Chem. Phys.* **1997**, *100*, 1.
- Yarkony, D. R. *Acc. Chem. Res.* **1998**, *31*, 511.
- Köppel, H.; Domcke, W. In *Encyclopedia of Computational Chemistry*; Schleyer, P. v. R., Ed.; Wiley: New York, 1998.
- Bersuker, I. B.; Polinger, V. Z. *Vibronic Interactions in Molecules and Crystals*; Springer: Berlin, 1989.
- Englman, R. *The Jahn–Teller Effect in Molecules and Crystals*; Wiley: New York, 1972.
- Köppel, H.; Cederbaum, L. S.; Domcke, W. *J. Chem. Phys.* **1988**, *89*, 2023.
- Döscher, M.; Köppel, H. *Chem. Phys.* **1997**, *225*, 93.
- Mahapatra, S.; Cederbaum, L. S.; Köppel, H. *J. Chem. Phys.* **1999**, *111*, 10452.
- Wilson, E. B., Jr.; Decius, J. C.; Cross, P. C. *Molecular Vibrations*; Dover: New York, 1955.
- Thomas, R. K.; Thompson, H. W. *Proc. R. Soc. A* **1974**, *339*, 29.
- Leng, F. J.; Nyberg, G. L. *J. Chem. Soc., Faraday Trans. 2* **1977**, *73*, 1719.
- Bieri, G.; Burger, F.; Heilbronner, E.; Maier, J. P. *Helv. Chim. Acta* **1977**, *60*, 145. Parr, A. C.; Jason, A. J.; Stockbauer, R. *Int. J. Mass Spectrom. Ion Phys.* **1978**, *26*, 23.
- Yang, Z. Z.; Wang, L. S.; Lee, Y. T.; Shirley, D. A.; Huang, S. Y.; Lester, W. A., Jr. *Chem. Phys. Lett.* **1990**, *171*, 9.
- Baltzer, P.; Wannberg, B.; Lundqvist, M.; Karlsson, L.; Holland, D. M. P.; MacDonald, M. A.; von Niessen, W. *Chem. Phys.* **1995**, *196*, 551.
- Bawagan, A. D. O.; Ghanty, T. K.; Davidson, E. R.; Tan, K. H. *Chem. Phys. Lett.* **1998**, *287*, 61.
- Cederbaum, L. S.; Domcke, W.; Köppel, H. *Chem. Phys.* **1978**, *33*, 319.
- Woywod, C.; Domcke, W. *Chem. Phys.* **1992**, *162*, 349.
- Cederbaum, L. S. *J. Phys. B* **1975**, *8*, 290. von Niessen, W.; Schirmer, J.; Cederbaum, L. S. *Comput. Phys. Rep.* **1984**, *1*, 57.
- Frisch, M. J. et al. *GAUSSIAN 94*, Revision C.2; Gaussian, Inc.: Pittsburgh, PA, 1995.
- Meyer, H.-D.; Manthe, U.; Cederbaum, L. S. *Chem. Phys. Lett.* **1990**, *165*, 73; Manthe, U.; Meyer, H.-D.; Cederbaum, L. S. *J. Chem. Phys.* **1992**, *97*, 3199.
- Beck, M. H.; Jäckle, A.; Worth, G. A.; Meyer, H.-D. *Phys. Rep.* **2000**, *324*, 1.
- Worth, G. A.; Meyer, H.-D.; Cederbaum, L. S. *J. Chem. Phys.* **1996**, *105*, 4412.
- Worth, G. A.; Meyer, H.-D.; Cederbaum, L. S. *J. Chem. Phys.* **1998**, *109*, 3518; *Chem. Phys. Lett.* **1999**, *299*, 451.
- Raab, A.; Worth, G. A.; Meyer, H.-D.; Cederbaum, L. S. *J. Chem. Phys.* **1999**, *110*, 936.
- Lichten, W. *Phys. Rev.* **1967**, *164*, 131. Smith, F. T. *Phys. Rev.* **1969**, *179*, 111. O'Malley, T. F. *Adv. Atomic Mol. Phys.* **1971**, *7*, 223.
- Tanabe, K.; Saeki, S. *Bull. Chem. Soc. Jpn.* **1974**, *47*, 1847.
- Perrin, M. H.; Gouterman, M. *J. Chem. Phys.* **1967**, *46*, 1019. van der Waals, J. H.; Berghuis, A. M. D.; de Groot, M. S. *Mol. Phys.* **1967**, *13*, 301; *Ibid.* **1971**, *21*, 497. Stephens, P. J. *J. Chem. Phys.* **1969**, *51*, 1995. Zgierski, M. Z.; Pawlikowski, M. *ibid.* **1979**, *70*, 3444.
- Domcke, W.; Köppel, H.; Cederbaum, L. S. *Mol. Phys.* **1981**, *43*, 851.
- Cullum, J.; Willoughby, R. *Lanczos Algorithms for Large Symmetric Eigenvalue Problems*; Birkhäuser: Boston, 1985; Vols. I & II.
- Fang, J.-Y.; Guo, H. *J. Chem. Phys.* **1994**, *101*, 5831.
- Dunning, T. H., Jr. *J. Chem. Phys.* **1989**, *90*, 1007.
- Engel, V. *Chem. Phys. Lett.* **1992**, *189*, 76. Manthe, U.; Meyer, H.-D.; Cederbaum, L. S. *J. Chem. Phys.* **1992**, *97*, 9062.
- Duschinsky, F. *Acta Physicochim. URSS* **1937**, *7*, 551. Botter, R.; Dibeler, V. H.; Walker, J. A.; Rosenstock, H. M. *J. Chem. Phys.* **1966**, *44*, 1271.
- Note the typographical error in the argument of the square root in eq 15 of ref 17.
- Gadea, F. X.; Köppel, H.; Schirmer, J.; Cederbaum, L. S.; Randall, K. J.; Bradshaw, A. M.; Ma, Y.; Sette, F.; Chen, C. T. *Phys. Rev. Lett.* **1991**, *66*, 883. Köppel, H.; Gadea, F. X.; Klatt, G.; Schirmer, J.; Cederbaum, L. S. *J. Chem. Phys.* **1997**, *106*, 4415.
- Dobrodey, N. V.; Köppel, H.; Cederbaum, L. S. *Phys. Rev. A* **1999**, *60*, 1988.